HHS Public Access

Author manuscript

ACS Sens. Author manuscript; available in PMC 2020 May 24.

Published in final edited form as:

ACS Sens. 2019 May 24; 4(5): 1230–1235. doi:10.1021/acssensors.8b01645.

Quiet Outer Membrane Protein G (OmpG) Nanopore for Biosensing

Raghavendar Reddy Sanganna Gari[‡,#], **Patrick Seelheim**[‡], **Binyong Liang**, and **Lukas K. Tamm**[*]

Department of Molecular Physiology and Biological Physics, Center for Cell and Membrane Physiology at the University of Virginia, Charlottesville, Virginia 22908, United States

Abstract

Interest in nanopore technology has been growing due to nanopores' unique capabilities in small molecule sensing, measurement of protein folding, and low-cost DNA and RNA sequencing. The *E. coli* β-barrel outer membrane protein OmpG is an excellent alternative to other protein nanopores because of its single polypeptide chain. However, the flexibility of its extracellular loops ultimately limits applications in traditional biosensing. We deleted several residues in and near loop 6 of OmpG. The dynamic structure of the new construct determined by NMR shows that loops 1, 2, 6, and 7 have reduced flexibilities compared to those of wild-type. Electrophysiological measurements show that the new design virtually eliminates flickering between open and closed states across a wide pH range. Modification of the pore lumen with a copper chelating moiety facilitates detection of small molecules. As proof of concept, we demonstrate concurrent single-molecule biosensing of glutamate and adenosine triphosphate.

Graphical Abstract

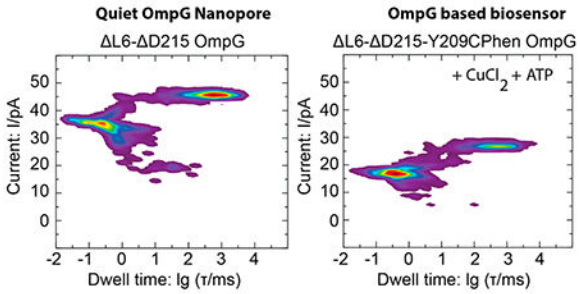

[*]**Corresponding Author**: Lkt2e@virginia.edu; Phone: +1-434-982-3578.

Author Contributions

The manuscript was written through contributions of all authors. All authors have given approval to the final version of the manuscript

[#]Present Address

Department of Anesthesiology, Weill Cornell Medicine, New York, NY 10065, United States. (R.R.S.G.)

[‡]R.R.S.G. and P.S. contributed equally.

Supporting Information

The Supporting Information is available free of charge on the ACS Publications website at DOI: 10.1021/acssensors.8b0145.

The authors declare no competing financial interest.

Keywords

outer membrane protein; OmpG; nanopore; biosensor; electrophysiology; black lipid membrane; NMR

Biotechnology is taking advantage of biological nanopores for low-cost DNA and RNA sequencing,[1,2] detection of small molecules,[3] polymers,[4] polypeptides,[5] and protein folding.[6] Among many channels, α-hemolysin is widely used for this purpose.[3] However, its heptameric structure poses an obstacle for fine-tuning the properties of the channel.[7] Recently, the *E. coli* outer membrane protein G (OmpG) has been considered as an excellent alternative.[8] OmpG nanopores are promising due to their stability and monomeric nature allowing easy and precise modification without requiring heteromeric assembly and additional purification steps.[9] X-ray and NMR structures reveal that OmpG is a 14-stranded β-barrel with 7 extracellular loops and 6 periplasmic short turns.[10–13] Gating of OmpG is controlled by highly dynamic extracellular loops, particularly loop 6, in a pH-dependent manner. The crystal structure of OmpG at pH 5.6 shows a closed conformation with loop 6 collapsed into the lumen, whereas at pH 7.5, OmpG adopts an open conformation with loop 6 extending away from the lumen.[13] At neutral pH, OmpG flickers between open and closed states. The pH dependency and flickering create obstacles for the practical use of OmpG as a biosensor. Several strategies have been used to create quiet OmpG nanopores: (i) β-strands 12 and 13 were cross-linked by a disulfide bond, and the irregularly positioned residue D215 was deleted creating an open pore at pH 5.0 and 7.0;[9] (ii) individual loops were pinned to the lipid bilayer through long hydrocarbon-chain alkylation with pinning of loop 6 reducing the gating activity by 95% at pH 6.0;[14] and (iii) loop 6 was shortened by 8 or 12 residues resulting in 63 or 81% reductions of spontaneous pore closings at pH 7.4, respectively.[15] However, the use of cysteine modifications in the design of some quiet channels14,16 hampers the ability for site-specific modification using cysteine chemistry for biosensing applications. Therefore, there is an unmet need for designing a single polypeptide nanopore that allows for facile detection of single small biomolecules. Here, we develop and structurally and functionally characterize a new nanopore that eliminates current flickering over a wide range of pH values and that is capable of simultaneously detecting and distinguishing single molecules of glutamate and adenosine triphosphate (ATP).

DESIGN OF QUIET OMPG NANOPORE

In our pursuit to engineer better quiet OmpG nanopores, we systematically investigated several OmpG constructs: (a) a truncation of loop 6 with residues 221-227 deleted and arginine 228 changed to a glycine (ΔL6 OmpG), (b) a deletion of the irregularly positioned aspartate 215 (ΔD215), and (c) a combination of ΔL6 and ΔD215 (ΔL6-ΔD215 OmpG). Supplementary Figures 1 and 2 show sequence alignments of wild-type and mutant OmpGs and their successful refolding in β-octylglucoside (β-OG). ΔD215 was targeted, because it forms a destabilizing bulge in the β-barrel structure that is eliminated by its deletion. Both ΔL6 OmpG and ΔD215 OmpG exhibited less flickering of their single-channel current at pH 7.4 and 8.5 than wild-type OmpG (Supplementary Figure 3). These results are consistent with those of previous reports.[9,15] However, at pH 6.0, ΔL6 OmpG still exhibited some

flickering, and the flickering of ΔD215 OmpG was not improved from wild-type OmpG (Supplementary Figure 3). In contrast, the ΔL6-ΔD215 combination mutant of OmpG showed no significant spontaneous pore closings over a wide pH range from 6.0 to 8.5 (Figure 1A) compared to wild-type OmpG, which frequently flickered between open and closed states (Figure 1B). To quantitatively evaluate single-channel recordings, we calculated nonparametric, unbiased, bin-free, 2D current versus dwell time histograms from long (>15 min) current traces (see Experimental Methods and ref 17, examples of longer traces are shown in Supplementary Figure 4). “Dwell time” is defined as the time the pore spends in any state (i.e., open or blocked (state that is at least partially blocked)). The resulting histograms showed probability densities (PDs) presented in Figure 1C,D for wild-type and double mutant, respectively. For wild-type at pH 7.4, the open state current PD was prominent at ~45 pA, and the PDs for the blocked states ranged from ~20 to 35 pA, reflecting much spontaneous gating. The prominent dwell times were on the order of 10 to 100 ms for the open state and on the order of 1 to 10 ms for the blocked state. The open state current PD of ΔL6-ΔD215 OmpG was similar to that of wild-type, but the PD for the blocked state current was more localized to ~35 pA, indicating less spontaneous gating. Importantly prominent dwell times of the open state were increased 10- to 100-fold from ~100 to 10 000 ms in ΔL6-ΔD215 compared to wild-type OmpG. At the same time, the spontaneous gating occurred far less frequently, and the prominent dwell times of the blocked states were reduced to 10 μs to 1 ms. We further calculated difference maps between 2D PD histograms of wild-type and ΔL6-ΔD215 OmpG (Figure 1E) for quantitative representation. In this map, the PDs in blue (negative) denote states that disappear when moving from wild-type to ΔL6-ΔD215 OmpG, whereas the PDs in red (positive) denote states that appear. It is very clear from this data (Figure 1E) that the ΔL6-ΔD215 double mutation increases the dwell time of the open state to tens of seconds and reduces the lifetime of the blocked state(s) to the microseconds range. Analogous difference maps between ΔD215 and wild-type OmpG, as well as ΔL6 and wild-type OmpG show that these single-mutant constructs only slightly enhanced the open state dwell times in comparison to wild-type OmpG (Supplementary Figure 3). However, both single-mutant OmpGs reduced the blocked state dwell times. Overall, ΔL6-ΔD215 OmpG stands out in terms of its much-improved open state lifetime.

NMR STUDIES OF QUIET OMPG NANOPORE

To investigate the effect of the ΔL6-ΔD215 double mutation on the structure of OmpG, we recorded ^{15}N-^{1}H transverse relaxation optimized heteronuclear single-quantum coherence (TROSY-HSQC) spectra of ^{2}H-,^{13}C-, and ^{15}N-labeled ΔL6-ΔD215 OmpG in DPC micelles (Supplementary Figure 5). We assigned the HN, N, CA, CB, and CO resonances based on TROSY-type through-bond triple-resonance (HNCA, HN(CA)CB, HNCO, and HN(CA)CO) NMR experiments. We then calculated the composite chemical shift changes between ΔL6-ΔD215 and wild-type OmpG. Resonance assignments of wild-type OmpG have been previously reported by our laboratory.[11] The chemical shift perturbations were large in β-strands 9 and 10 (Figure 2A). The double mutation largely affected the following residues: T144 and Y146 in loop 4, V151 and T155 in strand 8, L173, E174, and R175 in strand 9, G176 in loop 5, T190, Q191, E192, I193, and R194 in strand 10, G228 (G237 in wild-type)

in strand 12, and E254 (E263 in wild-type) in loop 7. Among all residues, the chemical shift change for E192 was largest (1.9 ppm). We note that all residues exhibiting large chemical shift changes are located structurally close to loop 6. Therefore, it appears that this double mutation strongly affected the local conformation near or at loop 6 without affecting the overall fold and integrity of the OmpG pore. In contrast, chemical shift differences between ΔL6 and wild-type OmpG were negligible (Supplementary Figure 6).

To further probe the effect of the double mutation, we calculated the solution NMR structure of ΔL6-ΔD215 OmpG based on 283 measured NOEs, 334 dihedral angle restraints, and 104 hydrogen bond restraints (see Experimental Methods). To compare this structure with that of wild-type, we recalculated the wild-type structure using the previously measured 316 NOEs, the 362 newly calculated dihedral restraints using TALOS-N, and the 110 hydrogen bond restraints using the data of Liang and Tamm.[11] NMR ensembles of the 10 calculated lowest-energy structures for both proteins are shown in Figure 2B–E. We next calculated and compared the residual mean square displacement (RMSD) values of individual loops and the β-barrel for both proteins (Supplementary Table 1). The RMSDs of the β-barrel were very similar for both proteins, indicating that overall fold and integrity of the barrel is similar. However, the RMSDs of the individual loops varied between two constructs. The RMSDs of loops 1, 2, and 7 were lower in ΔL6-ΔD215 than in wild-type OmpG. However, the RMSDs of loops 3, 4, and 5 were higher in ΔL6-ΔD215 than in wild-type OmpG. The RMSD of loop 6 is much lower in ΔL6-ΔD215. However, we note that this difference is expected due to the smaller number of residues in loop 6 of the mutant. Clearly, modification of OmpG in or near loop 6 also altered the dynamics of other near and distant loops. This change in loop dynamics is likely responsible for an altered spontaneous gating pattern resulting in a predominantly open nanopore of the mutant over a wide range of pH values as observed in our electrophysiology experiments. Broad dynamic distributions of loops 6 and 7 constrict the channel in wild-type but not in the mutant. Therefore, it is possible that, in addition to the main gating loop 6, loop 7 might also play an important role in the pH gating of wild-type OmpG. Even though many residues in strands 8, 9, and 10 showed large chemical shift changes, we did not observe a significant difference in the barrel structure. This might be due to the limited number of NOE restraints leading to a resolution not high enough to reveal small local structural changes in the barrel.

PROOF OF CONCEPT FOR BIOSENSING

Our electrophysiology and complementary NMR results showed that the ΔL6-ΔD215 OmpG mutant is quiet, making it an excellent candidate for applications in biosensing. In this current work, we mutated the inside-facing residue tyrosine 209 to a cysteine. This residue was chosen, because it is located in the center of the pore lumen. The Y209C mutation itself had no effect on the open state current and on dwell times of either open or blocked states of the ΔL6-ΔD215 OmpG pore (Supplementary Figure 7A,B). However, the current in the blocked state was slightly reduced. We then reacted the ΔL6-ΔD215-Y209C OmpG with *N*-(1,10-phenanthrolin-5-yl) iodoacetamide to allow binding of Cu^{2+} ions as a transducer for biosensing. ΔL6-ΔD215-Y209Cphen OmpG was successfully refolded into β-OG (Supplementary Figure 8). In comparison to ΔL6-ΔD215-Y209C OmpG, the open state current is slightly reduced in ΔL6-ΔD215-Y209Cphen OmpG, and the blocked state current

is slightly increased (Supplementary Figure 7B,C, see also Supplementary Figure 9 for sample current recordings of nanopores with phenanthroline). Open state dwell times remained the same; however, the blocked states dwell times were slightly increased. Next, we measured single-channel recordings of ΔL6-ΔD215-Y209Cphen OmpG in the presence of Cu^{2+} ions. Cu^{2+} ions serve as transducers by causing a permanent, partial blockage of the open state. For instance, both open (~40 vs ~25pA) and blocked state (~30 vs ~15 pA) currents of the ΔL6-ΔD215-Y209Cphen construct (Figure 3A,B and Supplementary Figure 7C,E) were reduced upon Cu^{2+} binding. This effect is completely reversible after removal of Cu^{2+} by chelation with EDTA (Supplementary Figure 7E,G). When Cu^{2+} ions were present during the single-channel recordings of ΔL6-ΔD215-Y209C OmpG (Supplementary Figure 7B,D), open and blocked states currents were the same as those of ΔL6-ΔD215 OmpG. However, a slight decrease of the open state lifetime was observed. Again, this effect is completely reversible after chelating Cu^{2+} (Supplementary Figure 7D,F).

We next tested if ΔL6-ΔD215-Y209Cphen OmpG with Cu^{2+} could be used for biosensing small molecules. As only two of the four coordination sites of Cu(II) are bound to phenanthroline, we expect that further interaction with compounds bearing vicinal hydroxyl or oxo groups should alter the current-dwell time distribution of ΔL6-ΔD215-Y209Cphen OmpG with Cu^{2+}. As physiologically relevant small molecules, we chose L-glutamate and ATP. Figure 3 shows the current-dwell time distributions of ΔL6-ΔD215-Y209Cphen OmpG in the presence of $CuCl_2$, ATP, glutamate, or a mixture of ATP and glutamate, as well as the respective difference maps compared to $CuCl_2$ alone. The presence of ATP (Figure 3C,D) leads to a small but distinct reduction of the blocked state current while also slightly lowering the probability density of the open state. In contrast, L-glutamate (Figure 3E,F) did not cause a reduction in blocked state current but led to a pronouncedly lower open state probability and the appearance of a spread-out probability density on the 1 to 10 ms time scale. In the presence of both ATP and L-glutamate (Figure 3G,H), both patterns can be observed in the PD difference map, showing that measurements of these two analytes are approximately additive. In contrast, controls with unsensitized ΔL6-ΔD215-Y209C OmpG nanopores did not show differences between $CuCl_2$ alone and ATP + L-glutamate (Supplementary Figure 10, see also Supplementary Figure 11 for sample current recordings of negative control nanopores without phenanthroline). These data prove that this single-molecule biosensor simultaneously detects and distinguishes between ATP and L-glutamate.

Phenanthroline has been previously introduced as an adaptor in α-hemolysin nanopores.[18,19] Because of the heptameric structure of this protein, this required mixing monomers with and without the adaptor in a 1:6 ratio and selecting pores from the binomial distribution that had just a single adaptor. Our new design with the monomeric OmpG nanopore does not require assembly from two different molecules and selection of the correct stoichiometry. As in α-hemolysin, ATP blocked more current than L-glutamate in the OmpG nanopore. However, current block dwell times in the OmpG nanopore for both analytes are smaller (in the range of 100 μs to 1 ms for ATP and 100 μs to 10 ms for L-glutamate) in comparison to those of α-hemolysin nanopores (10 to 100 ms for ATP and 10 to 1000 ms for L-glutamate).[18] However, we note that the pore size of the OmpG is narrower (elliptical in cross section with dimensions of 15 × 12 Å) compared to the pore size in α-hemolysin (>20 Å).[13] Moreover,

charge distribution across the constriction might be different in these two nanopores. Therefore, these factors may influence measured dwell times.

CONCLUSION

In this work, we developed a quiet OmpG nanopore with negligible spontaneous gating across a wide pH range that can be functionalized using cysteine chemistry. The presented solution NMR structure should guide future designs for singlemolecule biosensing. The biosensor is capable of detecting and distinguishing between individual single small molecules such as ATP and L-glutamate. We expect that this platform will be useful for developing future biosensors to detect a wide range of molecules at the single-molecule level.

EXPERIMENTAL METHODS

Expression, Purification, and Refolding of OmpG Constructs

The plasmid pT7-SMC-ompG encoding for mature OmpG was a kind gift from Dr. H. Bayley (Oxford University, Oxford, U.K.).[20] Deletions and point mutations were introduced by successive rounds of site-directed mutagenesis using respective primer pairs (Supplementary Table 2). Expression of OmpG constructs into inclusion bodies in *E. coli* and subsequent purification and refolding into *n*-octyl-*β*-D-glucoside (*β*-OG) for electrophysiology and dodecylphosphocholine (DPC) for NMR were performed as previously described,[11] except that probe sonication (model CL-18, 80% amplitude, 20 s on/40 s off, 15 min, 4 °C) was used for mechanical cell lysis instead of a French press and that 1 mM DTT was added to the denaturation buffer (8 M urea, 10 mM Tris-HCl pH 8.0, 0.1 mM EDTA) for all constructs with cysteines.

Phenanthroline Labeling of Y209C Mutants

OmpG-ΔL6-ΔD215-Y209C was labeled after purification in denaturation buffer before refolding. The protein concentration was adjusted to approximately 0.5 mM, and an aliquot was reduced with a 10-fold molar excess of DTT for 1 h at RT. After removal of DTT by gel filtration over Sephadex G-25 using degassed denaturation buffer without DTT as eluent, the sample was reacted with a 100-fold molar excess of 5-iodoacetamido-*N*-1,10-phenanthroline (250 mM in anhydrous dimethylformamide) in the presence of 10% dimethylformamide for 1 h at RT in the dark with constant mixing. Unreacted labeling reagent was removed by gel filtration over Sephadex G-25 using regular denaturation buffer without DTT as eluent. The sample was concentrated to its original volume (10 kDa MWCO centrifugal concentrator) and refolded as described above.

Electrophysiology on Planar Lipid Bilayers

Single-molecule electrophysiology recordings were performed on solvent-free Montal-Mueller black-lipid membranes using an Axopatch 200A patch-clamp amplifier interfaced to a computer via a NI USB-6356 digitizer and a homemade LabVIEW program for data acquisition.

The two compartments of homemade sample chambers (a kind gift of Dr. H. Bayley[21]) were separated by a 25 μm thick PTFE membrane (Goodfellow, USA), in which a round aperture of approximately 100 μm diameter had been created by high-voltage spark discharge (precision spark generator, USA). The aperture was painted with *n*-hexadecane (5 μL, 1% (v/v) in *n*-pentane. After complete evaporation of the solvent, both chambers were filled with 1 M KCl buffered with either 10 mM Bis-Tris at pH 6.0 or 10 mM Tris-HCl at pH 7.4 and 8.5, respectively, and connected to Ag/AgCl electrodes by salt bridges (3 M KCl in 3% agarose). Monolayers of DPhPC were formed on the air-water interface of both compartments from 10 mg/mL DPhPC in *n*-pentane, and the solvent was allowed to completely evaporate during 30 min. Lowering and raising the liquid level in both compartments led to the formation of a planar lipid bilayer covering the aperture.

OmpG was added to one compartment from a nanomolar solution in β-OG, and a voltage of 100 mV was applied to facilitate insertion. After insertion of a single OmpG, uninserted OmpG was removed by perfusion at zero voltage. Current traces were then recorded at 40 mV with a 5 kHz low-pass filter and 50 kHz sampling rate.

Current states and their dwell times were determined in WinEDR (University of Strathclyde UK) and bin-free, nonparametric, two-dimensional current vs dwell time distributions were calculated in Matlab by adaptive kernel density estimation.[17] Probability density histograms were generated from traces that were mostly 15 min long and in a few cases a little longer.

NMR Spectroscopy

^{2}H-, ^{15}N-, and ^{13}C-labeled protein samples were refolded in β-OG and then exchanged into DPC micelles. All NMR experiments were recorded at 40 °C on a Bruker Avance III 800 spectrometer equipped with a triple-resonance cryoprobe. All double- and triple-resonance experiments were performed using the Bruker Topspin version 2.1.6 software suite. Sequential backbone assignments for both ΔL6-ΔD215 OmpG and ΔL6 OmpG were obtained by recording TROSY versions of HNCA, HN(CA)CB, HNCO, and HN(CA)CO experiments. 3D ^{15}N-edited ^{15}N-^{1}H-^{1}H NOESY-TROSY and ^{15}N-^{1}H-^{15}N HSQC-NOESY-HSQC experiments with mixing times of 200 ms were recorded to obtain NOEs for ΔL6-ΔD215 OmpG. NMR data were processed with NMRPipe and analyzed with Sparky software.[25]

NMR Structure Calculations

For ΔL6-ΔD215 OmpG, distance constraints were calibrated and calculated manually based on an average distance of 3.3 Å between β-strands. Backbone dihedral angle constraints were determined from chemical shifts corrected for deuterium and TROSY effects using TALOS-N.[22] Hydrogen bond constraints were only applied to observed strong NOE pairs using the same criteria as in wild-type. Structure calculations were performed using CNS version 1.2[23] using 4000 high-temperature, 8000 torsion slow-cool, and 8000 Cartesian slow-cool annealing steps. A total of 200 structures were calculated, and the 10 lowest-energy structures were selected for ensemble analysis. Ramachandran plot statistics as calculated with PROCHECK-NMR[24] showed residues in the most favored (72.3%), additionally allowed (22.8%), generously allowed (3.3%), and disallowed (1.5%) regions.

For wild-type OmpG, NOEs and hydrogen bond constraints were taken directly from our previous report.[11] However, backbone dihedral angle constraints were recalculated with TALOS-N from our previously published chemical shifts.[11] Structures were then calculated using the same procedures described above for the mutant. Ramachandran plot statistics as calculated with PROCHECK-NMR[24] showed residues in the most favored (70.4%), additionally allowed (25.1%), generously allowed (3.1%), and disallowed (1.4%) regions.

Supplementary Material

Refer to Web version on PubMed Central for supplementary material.

ACKNOWLEDGMENTS

This work was supported by NIH grant R01 GM051329 to L.K.T.

ABBREVIATIONS

DNA	deoxyribonucleic acid
RNA	ribonucleic acid
***α*HL**	*α*-hemolysin
E. coli	*Escherichia coli*
NMR	nuclear magnetic resonance
ATP	adenosine triphosphate
DPhPC	1,2-diphytanoyl-*sn*-glycero-3-phosphocholine
PD	probability density
TROSY-HSQC	transverse relaxation optimized hetero-nuclear single-quantum coherence
NOE	nuclear overhauser effect
RMSD	residual mean square displacement
L-Glu	L-glutamate
$CuCl_2$	copper(II) chloride
DTT	dithiothreitol
RT	room temperature
MWCO	molecular weight cutoff
DPC	*n*-dodecylphosphocholine

REFERENCES

(1). Stoddart D; Heron AJ; Mikhailova E; Maglia G; Bayley H Single-nucleotide discrimination in immobilized DNA oligonucleotides with a biological nanopore. Proc. Natl. Acad. Sci. U. S. A 2009, 106 (19), 7702–7707. [PubMed: 19380741]

(2). Ayub M; Hardwick SW; Luisi BF; Bayley H Nanopore-based identification of individual nucleotides for direct RNA sequencing. Nano Lett. 2013, 13 (12), 6144–6150. [PubMed: 24171554]

(3). Bayley H; Cremer PS Stochastic sensors inspired by biology. Nature 2001, 413 (6852), 226–230. [PubMed: 11557992]

(4). Boukhet M; König NF; Ouahabi AA; Baaken G; Lutz J; Behrends JC Translocation of precision polymers through biological nanopores. Macromol. Rapid Commun 2017, 38 (24), 1700680.

(5). Wu D; Bi S; Zhang L; Yang J Single-molecule study of proteins by biological nanopore sensors. Sensors 2014, 14 (10), 18211–18222. [PubMed: 25268917]

(6). Rodriguez-Larrea D; Bayley H Multistep protein unfolding during nanopore translocation. Nat. Nanotechnol 2013, 8 (4), 288–295. [PubMed: 23474543]

(7). Song L; Hobaugh MR; Shustak C; Cheley S; Bayley H; Gouaux JE Structure of staphylococcal α-hemolysin, a heptameric transmembrane pore. Science 1996, 274 (5294), 1859–1865. [PubMed: 8943190]

(8). Eisenberg B Engineering channels: Atomic biology. Proc. Natl. Acad. Sci. U. S. A 2008, 105 (17), 6211–6212. [PubMed: 18443300]

(9). Chen M; Khalid S; Sansom MS; Bayley H Outer membrane protein G: Engineering a quiet pore for biosensing. Proc. Natl. Acad. Sci. U. S. A 2008, 105 (17), 6272–6277. [PubMed: 18443290]

(10). Subbarao GV; van den Berg B Crystal structure of the monomeric porin OmpG. J. Mol. Biol 2006, 360 (4), 750–759. [PubMed: 16797588]

(11). Liang B; Tamm LK Structure of outer membrane protein G by solution NMR spectroscopy. Proc. Natl. Acad. Sci. U. S. A 2007, 104 (41), 16140–16145. [PubMed: 17911261]

(12). Retel JS; Nieuwkoop AJ; Hiller M; Higman VA; Barbet-Massin E; Stanek J; Andreas LB; Franks WT; van Rossum B; Vinothkumar KR; Handel L; de Palma GG; Bardiaux B; Pintacuda G; Emsley L; Kuhlbrandt W; Oschkinat H Structure of outer membrane protein G in lipid bilayers. Nat. Commun 2017, 8 (1), 2073. [PubMed: 29233991]

(13). Yildiz O; Vinothkumar KR; Goswami P; Kuhlbrandt W Structure of the monomeric outer-membrane porin OmpG in the open and closed conformation. EMBO J. 2006, 25 (15), 3702–3713. [PubMed: 16888630]

(14). Zhuang T; Tamm LK Control of the conductance of engineered protein nanopores through concerted loop motions. Angew. Chem, Int. Ed 2014, 53 (23), 5897–5902.

(15). Grosse W; Psakis G; Mertins B; Reiss P; Windisch D; Brademann F; Bürck J; Ulrich A; Koert U; Essen L Structure-based engineering of a minimal porin reveals loop-independent channel closure. Biochemistry 2014, 53 (29), 4826–4838. [PubMed: 24988371]

(16). Perez-Rathke A; Fahie MA; Chisholm C; Liang J; Chen M Mechanism of OmpG pH-dependent gating from loop ensemble and single channel studies. J. Am. Chem. Soc 2018, 140 (3), 1105–1115. [PubMed: 29262680]

(17). Botev ZI; Grotowski JF; Kroese DP Kernel density estimation via diffusion. Annals of Statistics. 2010, 38 (5), 2916–2957.

(18). Boersma AJ; Brain KL; Bayley H Real-time stochastic detection of multiple neurotransmitters with a protein nanopore. ACS Nano 2012, 6 (6), 5304–5308. [PubMed: 22616662]

(19). Boersma AJ; Bayley H Continuous stochastic detection of amino acid enantiomers with a protein nanopore. Angew. Chem 2012, 124 (38), 9744–9747.

(20). Conlan S; Zhang Y; Cheley S; Bayley H Biochemical and biophysical characterization of OmpG: A monomeric porin. Biochemistry 2000, 39 (39), 11845–11854. [PubMed: 11009596]

(21). Maglia G; Heron AJ; Stoddart D; Japrung D; Bayley H Analysis of single nucleic acid molecules with protein nanopores. Methods Enzymol. 2010, 475, 591–623. [PubMed: 20627172]

(22). Shen Y; Bax A Protein backbone and sidechain torsion angles predicted from NMR chemical shifts using artificial neural networks. J. Biomol. NMR 2013, 56 (3), 227–241. [PubMed: 23728592]

(23). Brunger AT; Adams PD; Clore GM; DeLano WL; Gros P; Grosse-Kunstleve RW; Jiang J; Kuszewski J; Nilges M; Pannu NS; et al. Crystallography & NMR system: A new software suite for macromolecular structure determination. Acta Crystallogr., Sect. D: Biol. Crystallogr 1998, 54 (5), 905–921. [PubMed: 9757107]

(24). Laskowski RA; Rullmann JAC; MacArthur MW; Kaptein R; Thornton JM AQUA and PROCHECK-NMR: Programs for checking the quality of protein structures solved by NMR. J. Biomol. NMR 1996, 8 (4), 477–486. [PubMed: 9008363]

(25). Goddard TD; Kneller DG Sparky 3; University of California, San Francisco.

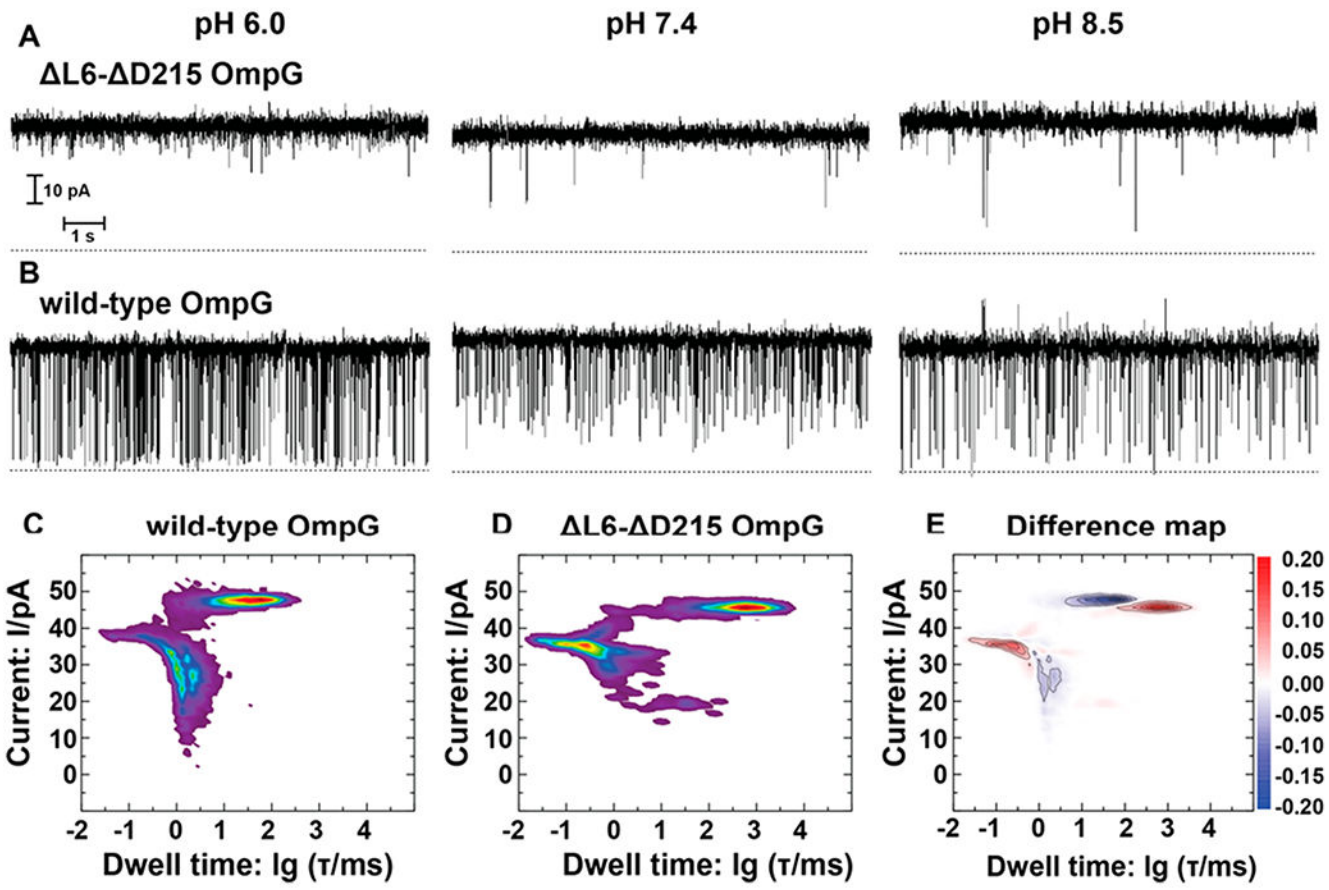

Figure 1.

Electrophysiological characteristics of wild-type and ΔL6-ΔD215 OmpG. (A) Segments of 10 s from representative current traces at −40 mV of a single ΔL6-ΔD215 OmpG in a DPhPC black-lipid membrane in 1 M KCl buffered at the indicated pH values. (B) Segments of 10 s from representative current traces of a single wild-type OmpG under the same conditions as in panel A. (C) Probability density histogram of current versus dwell time distribution from at least 15 min of single-channel recordings of wild-type OmpG at pH 7.4. (D) Probability density histogram of current versus dwell time distribution from at least 15 min of single-channel recordings of ΔL6-ΔD215 OmpG at pH 7.4. (E) Difference map of D – C to visualize changes in the current versus dwell time distributions between ΔL6-ΔD215 and wild-type OmpG at pH 7.4.

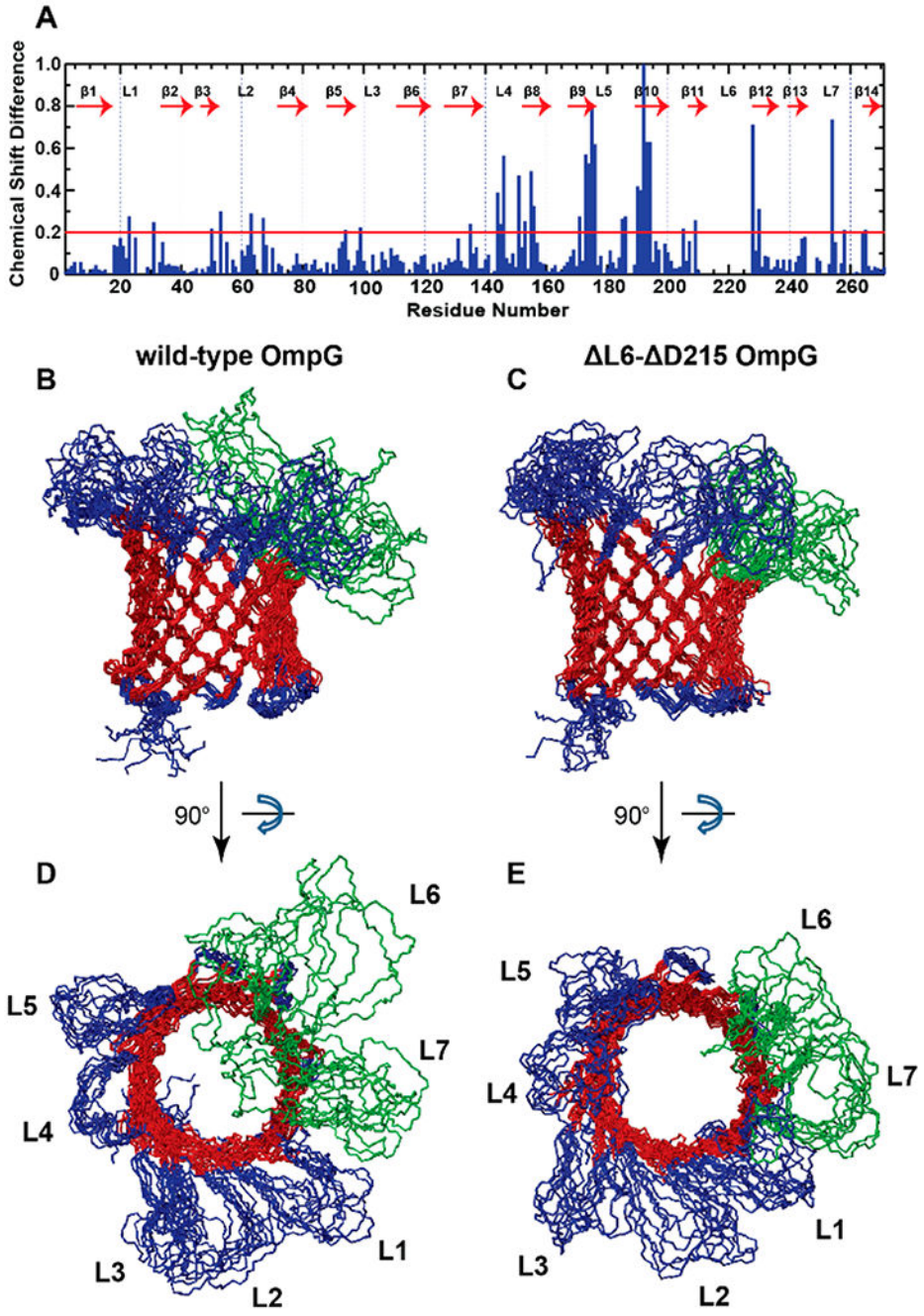

Figure 2.

Structural and dynamical changes between wild-type and mutant OmpG. (A) Chemical shift changes between ΔL6-ΔD215 and wild-type OmpG. A red line is drawn at 0.2 ppm, which is 5-fold higher than the estimated average measuring error. (B,D) NMR ensemble of the 10 lowest-energy structures of wild-type OmpG in side-view (B) and top-down view (D). (C,E) NMR ensemble of the 10 lowest-energy structures of ΔL6-ΔD215 OmpG in side-view (C) and top-down view (E). β-sheet residues are shown in red, N- and C-termini, periplasmic

turns, and loops 1 to 5 are shown in blue, and loops 6 and 7 are shown in green. The β-sheet residues were used for superposition of the structures.

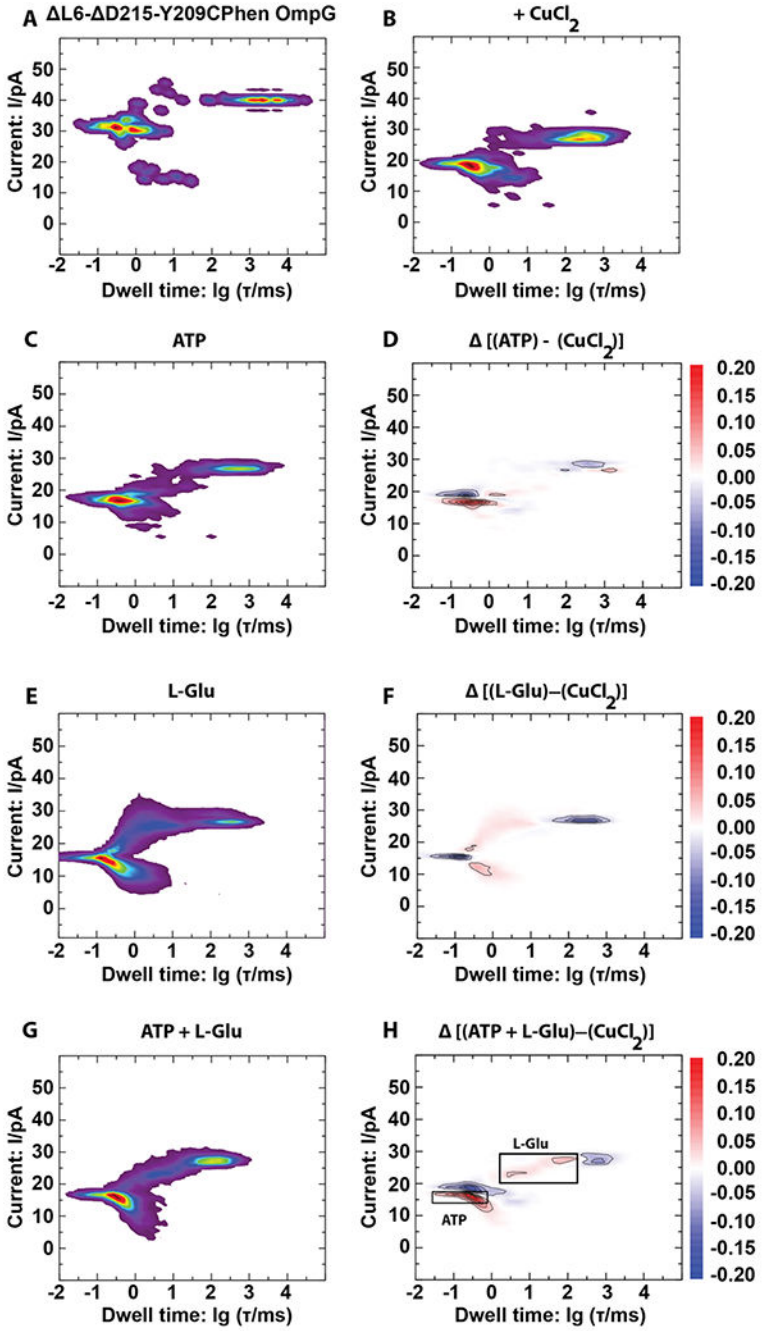

Figure 3.

Sensing ATP and L-glutamate with a single Cu^{2+}-ΔL6-ΔD215-Y209C-phenanthroline OmpG. Probability density histograms of current versus dwell time distributions of single ΔL6-ΔD215-Y209C-phenanthroline OmpG (A), ΔL6-ΔD215-Y209C-phenanthroline OmpG + 10 μM $CuCl_2$ (B), ΔL6-ΔD215-Y209C-phenanthroline OmpG + 10 μM $CuCl_2$ + 20 μM ATP (C), ΔL6-ΔD215-Y209C-phenanthroline OmpG + 10 μM $CuCl_2$ + 20 μM L-Glu (E), and ΔL6-ΔD215-Y209C-phenanthroline OmpG + 10 μM $CuCl_2$ + 20 μM ATP + 20 μM L-Glu (G). Probability density histograms of current versus dwell time distributions for all

conditions were obtained from at least 15 min of recordings at −40 mV in a solvent-free DPhPC black-lipid membrane in 1 M KCl buffered at pH 7.4. Difference maps visualizing the changes due to the analytes being present are shown for ATP (D), L-Glu (F), and ATP + L-Glu (H).